Journal of Materials Chemistry C

ROYAL SOCIETY OF CHEMISTRY

PAPER

View Article Online
View Journal | View Issue

Cite this: J. Mater. Chem. C, 2025, 13, 2814

Side-chain regulated topology of 2D covalent organic frameworks and its impact on photocatalytic synthesis of H_2O_2†

Shuai Sun,[ab] Chao-Qin Han,*[b] Jia-Xin Guo,[ab] Lei Wang,[b] Ze-Yang Wang,[a] Gonghao Lu *[a] and Xiao-Yuan Liu *[b]

Received 19th September 2024,
Accepted 2nd December 2024

DOI: 10.1039/d4tc03991b

rsc.li/materials-c

The development of covalent organic frameworks (COFs) with efficient photocatalytic H_2O_2 generation and building the structure–performance relationships are essential to rationally design and construct COFs for photocatalysis. Herein, COFs with **kgm** and **fes** underlying nets were successfully prepared *via* tuning the side-chain length of organic building units to investigate topological effects on H_2O_2 photosynthesis. We found that an ethoxy group-based **fes** COF, HIAM-0023 (HIAM = Hoffmann Institute of Advanced Materials), exhibits a much higher H_2O_2 generation rate (149.5 μmol g^{-1} h^{-1}) than a non-substituted **kgm** type COF (68.9 μmol g^{-1} h^{-1}). Furthermore, an enhanced photocatalytic efficiency of 391.7 μmol g^{-1} h^{-1} is obtained using mixed-linker HIAM-0023 with 37.5% hydroxyl substitution. This work sheds light on the rational construction of COFs with controllable topologies and compositions to realize efficient H_2O_2 photosynthesis.

Introduction

As a class of new porous materials, covalent organic frameworks (COFs)[1–5] have gradually received extensive attention as photocatalysts for H_2O_2 generation.[6,7] It is thus very important to build structure–property relationships between COFs and their performances for photocatalytic H_2O_2 production, which will undoubtedly facilitate the rational design and construction of COFs to realize high efficiency and stability for H_2O_2 photosynthesis. Since 2020,[8] with respect to organic building units and their effect on the electronic structures of COFs, many efforts have been made to prepare COFs with different compositions and structures in order to achieve efficient photocatalytic efficiency for H_2O_2 generation.[9–20]

It has been reported that locations and numbers of nitrogen atoms in COFs, lengths of building units, and linkage microenvironments have shown significant effects on H_2O_2 generation rates of resultant COFs.[21–24] For example, Jiang *et al.* prepared three donor–acceptor COFs using non-conjugated hydrazine linkages, partially π-conjugated imine linkages and fully π-conjugated vinylene linkages, in which the COF possessing hydrazine linkages exhibits the best photocatalytic H_2O_2 generation performance with a rate of 5.7 mmol g^{-1} h^{-1} and an apparent quantum efficiency of 17.5% at 420 nm.[18] It has also been proven that molecular junctions in COFs can be utilized as a useful strategy to enhance the photocatalytic H_2O_2 production.[12,25] For example, Lan *et al.* constructed a COF with an oxidation–reduction molecular junction, which presents a record-high yield of 276 mmol g^{-1} h^{-1} for photocatalytic H_2O_2 generation without sacrificial agents.[12] Although great efforts have been made to investigate the structure–property relationships between COFs and their H_2O_2 production performances, no work has been done to investigate topological effects on the photocatalytic H_2O_2 generation performances of COFs. COFs with different topologies can be obtained *via* varying reaction conditions, such as solvents,[26–28] the aging process,[29] and monomer concentrations.[28,30] As an alternative approach, the side-chain on the skeleton of monomers has also been considered as a useful strategy to regulate the topologies of resultant COFs.[31–33]

Herein, to investigate the topological influence on the activity of H_2O_2 photosynthesis, COFs possessing **kgm** and **fes** underlying nets were constructed using N^1,$N^{1\prime}$-(benzo[*c*][1,2,5]thiadiazole-4,7-diyl)bis(N^1-(4-aminophenyl) benzene-1,4-diamine) (BTAPA) and terephthalaldehydes with different lengths of side chains, such as terephthalaldehyde (TPA), 2,5-diethoxyterephthalaldehyde (DETA), 2,5-dipropoxyterephthalaldehyde (DPTA) and 2,5-dibutoxyterephthalaldehyde (DBTA). The experimental results reveal that the condensation of BTAPA and TA led to the formation of a COF, HIAM-0022, with a dual-pore **kgm** structure, while the reactions of BTAPA with DETA or

[a] School of Chemical Engineering, University of Science and Technology Liaoning, 185 Qianshan Zhong Road, Anshan, 114051, P. R. China. E-mail: ghlu@ustl.edu.cn
[b] Hoffmann Institute of Advanced Materials, Shenzhen Polytechnic University, 7098 Liuxian Blvd, Nanshan District, Shenzhen, 518055, P. R. China. E-mail: hancq_lv@szpu.edu.cn, liuxiaoyuan1989@szpu.edu.cn

† Electronic supplementary information (ESI) available. See DOI: https://doi.org/10.1039/d4tc03991b

DPTA or DBTA resulted in generation of COFs with a single-pore **fes** structure, namely HIAM-0023, HIAM-0024 and HIAM-0025, respectively. HIAM-0023 exhibits a significantly higher H_2O_2 generation rate of 149.5 μmol g^{-1} h^{-1} compared to 68.9 μmol g^{-1} h^{-1} for HIAM-0022. In addition, an enhanced photocatalytic H_2O_2 generation performance of 391.7 μmol g^{-1} h^{-1} was realized *via* partial hydroxylation of HIAM-0023. This work sheds light on the rational design and synthesis of COFs with specific underlying nets and compositions to achieve enhanced photocatalytic activity.

Results and discussion

Construction and characterization of 2D-COFs with side-chain regulated topologies

To realize the topology evolution, a tetratamine-based organic building unit, N^1,$N^{1\prime}$-(benzo[*c*][1,2,5]thiadiazole-4,7-diyl)bis(N^1-(4-aminophenyl) benzene-1,4-diamine) (BTAPA), was synthesized *via* a four-step route and characterized by ^{1}H and ^{13}C NMR (detailed procedures are provided in the ESI,† Fig. S1–S6). BTAPA was used to react with terephthalaldehydes with different lengths of side chains, including terephthalaldehyde (TPA), 2,5-diethoxyterephthalaldehyde (DETA), 2,5-dipropoxyterephthalaldehyde (DPTA) and 2,5-dibutoxyterephthalaldehyde (DBTA) (Fig. 1a and b). In a typical synthetic protocol of COFs, 0.05 mmol BTAPA and 0.2 mmol corresponding dialdehyde were suspended in a mixture of *o*-dichlorobenzene and mesitylene with 17.5 M acetic acid in a sealed Pyrex tube, which reacted at 120 °C for 3 days to obtain black powders (named HIAM-0022 for BTAPA-TPA, HIAM-0023 for BTAPA-DETA, HIAM-0024 for BTAPA-DPTA and HIAM-0025 for BTAPA-DBTA).

The powder X-ray diffraction (PXRD) analysis and theoretical simulations were conducted to determine the structures and crystallinity of the four as-synthesized COFs. As shown in Fig. 1c, HIAM-0022 exhibits great PXRD patterns with peak positions at about 2.39° and 4.78°, which are very different from those for HIAM-0023 to HIAM-0025. The main peak positions for these three COFs are approximately at 4.60°, 6.51° and 9.19° (Fig. 1d–f). These results indicate that HIAM-0022 and the other three COFs possess different underlying nets. According to the PXRD patterns of these four COFs, simulations were carried out to obtain their exact structures. It should be noted that dual-pore (DP) or single-pore (SP) structures might be generated with eclipsed packing (AA) and staggered packing (AB) using such organic building units. For HIAM-0022, as depicted in Fig. 1c and g, the simulated PXRD patterns based on the DP-AA structure show excellent agreement with the experimental patterns. Meanwhile, for HIAM-0023 to HIAM-0025, the simulated PXRD patterns according to the SP-AA structures well-matched with the experimental patterns (Fig. 1d–h, e–i and f–g). Furthermore, negligible differences were observed between the profile of Rietveld refinement and experimental diffractions. As a result, HIAM-0022 possesses a **kgm** topology, in which the lattice parameters are $a = c = 43.6752$ Å, $b = 3.4977$ Å, $\alpha = \beta = 90°$ and $\gamma = 59.2°$ with final R_{wp} and R_p values of 3.77% and 4.39%. HIAM-0023, HIAM-0024 and HIAM-0025 possess a **fes** underlying net. The unit cell parameters are: $a = 32.2745$ Å, $b = 29.3605$ Å, $c = 4.7628$ Å, $\alpha = \gamma = 90°$, and $\beta = 91°$ with final R_{wp} and R_p values of 3.28% and 4.39% for HIAM-0023; $a = 30.7571$ Å, $b = 32.7385$ Å, $c = 4.6603$ Å, $\alpha = \gamma = 90°$, and $\beta = 90°$ with final R_{wp} and R_p values of 3.56% and 4.80% for HIAM-0024; $a = 31.7806$ Å, $b = 32.2379$ Å, $c = 4.4875$ Å, $\alpha = \gamma = 90°$, and $\beta = 90°$ with final R_{wp} and R_p values of 4.46% and 6.09% for HIAM-0025.

Fourier-transform infrared (FTIR) spectra were used to confirm the formation of the C=N band. As depicted in Fig. 2a and Fig. S7 (ESI†), these four COFs show a characteristic C=N stretching band around 1631 cm^{-1}. The vibration of the NH_2 group (~3450 cm^{-1}) in BTAPA and the aldehyde stretching (~1695 cm^{-1} for TPA, ~1680 cm^{-1} for DETA, ~1683 cm^{-1} for DPTA and ~1678 cm^{-1} for DBTA) were largely attenuated after condensation reactions. These results indicated a high degree of polymerization and the generation of imine bonds. The solid-state ^{13}C NMR spectra of these four COFs were also measured. The signals are around 153 and 155 ppm (Fig. S8, ESI†), which correspond to the C atom in the C=N bonds, further indicating the formation of HIAM-0022 to HIAM-0025. The morphologies and compositions of the four COFs were analysed using scanning electron microscopy (SEM) and energy dispersive X-ray spectroscopy (Fig. S9–S13, ESI†). The CO_2 adsorption–desorption analysis was performed to evaluate the porosity of HIAM-0022 and HIAM-0025. As depicted in Fig. S14 (ESI†), HIAM-0022 and HIAM-0025 show Type I isotherms with surface areas of 129.25, 556.82, 430.26 and 260.69 m^2 g^{-1} using the Brunauer–Emmett–Teller (BET) model. The corresponding pore size distributions are around 0.53 and 0.70 nm for HIAM-0022 and 0.83 nm for the other three COFs. These results further demonstrate the DP-AA structure for HIAM-0022 and the SP-AA structures for HIAM-0023 to HIAM-0025.

The chemical and thermal stabilities of HIAM-0022 to HIAM-0025 were analysed, which is essential for their practical applications. For HIAM-0022, the excellent agreement of the PXRD patterns of HIAM-0022 before and after treatment under various conditions (including in water at room temperature, pH = 4, 10 and 12 aqueous solutions for 24 hours) indicated its high chemical stability (Fig. S15a, ESI†). Meanwhile, under much harsher conditions, such as boiling water and pH = 2 aqueous solution, the long-range order of HIAM-0022 could be gradually broken. However, almost no changes were recorded for the PXRD patterns of HIAM-0023 to HIAM-0025 under all these tested conditions (Fig. S15b–d, ESI†), which demonstrate that the long-range orders of HIAM-0023 to HIAM-0025 were maintained very well. The well-matched FT-IR spectra before and after various treatments also indicate the high chemical stability of HIAM-0022 to HIAM-0025 (Fig. S16, ESI†). Thermogravimetric analysis (TGA) reveals that these four COFs exhibit excellent thermal stability up to about 460 °C for HIAM-0022 and about 400 °C for the other three COFs (Fig. S17, ESI†).

Optical properties and photocatalytic hydrogen peroxide production performances of HIAM-0022 to HIAM-0025

The solid-state photoluminescence and UV-vis diffuse reflection absorption spectra of HIAM-0022 to HIAM-0025 were

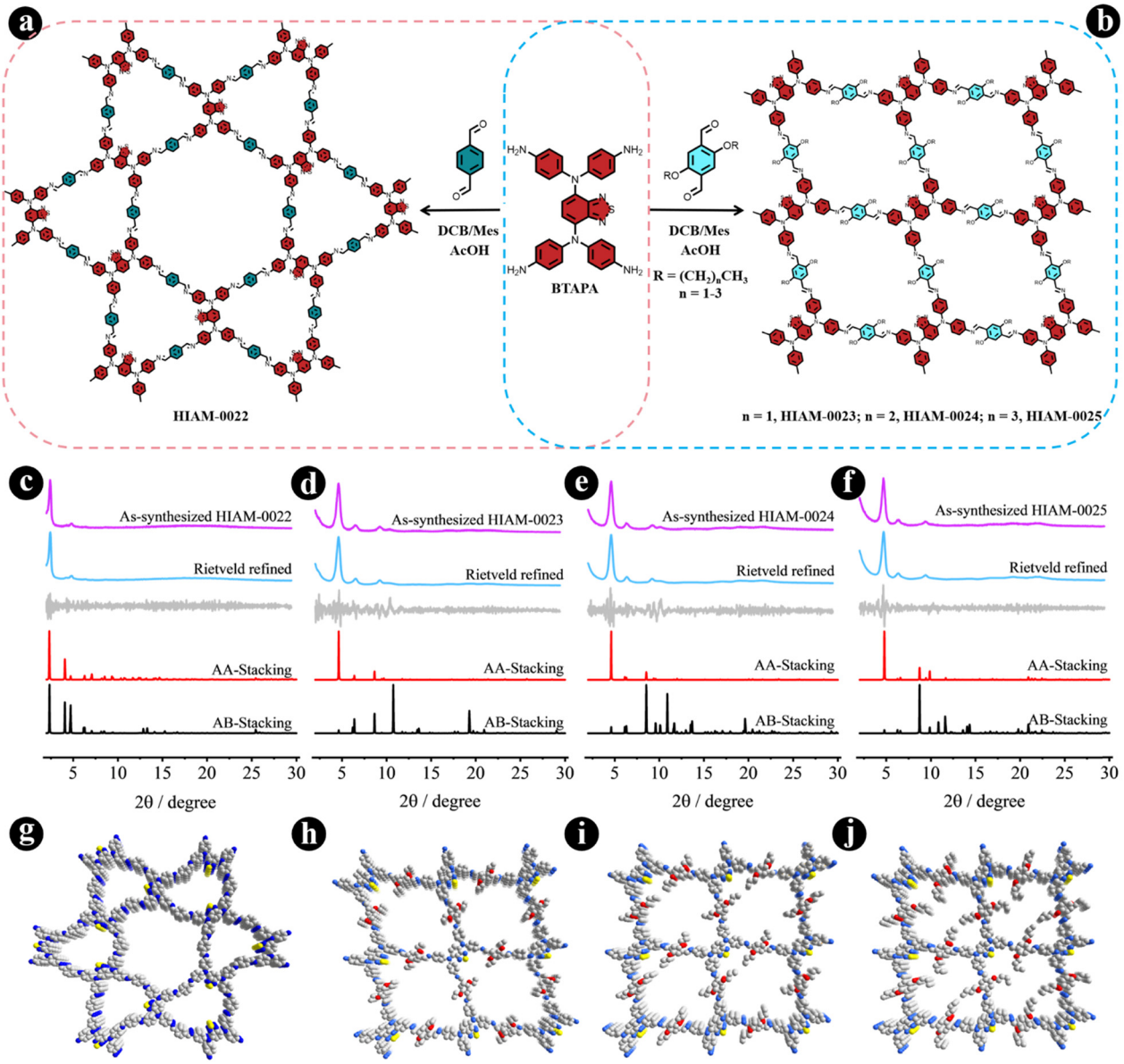

Fig. 1 Molecular structures of organic building units and synthesis conditions of HIAM-0022 (a) and HIAM-0023, HIAM-0024 and HIAM-0025 (b) COFs from BTAPA and dialdehydes with different lengths of side chains. Experimental PXRD patterns of as-synthesized COFs (purple line), Rietveld refinement (blue line), the difference (gray line), the simulated PXRD patterns based on AA-stacking (red line) and AB-stacking (black line) modes of HIAM-0022 (c), HIAM-0023 (d), HIAM-0024 (e) and HIAM-0025 (f). The top view of simulated AA stacking for HIAM-0022 (g), HIAM-0023 (h), HIAM-0024 (i) and HIAM-0025 (j).

recorded to investigate their optical behaviours. As shown in Fig. S18 (ESI†), the maximum emission peaks are about 783, 812, 826 and 806 nm for HIAM-0022, HIAM-0023, HIAM-0024 and HIAM-0025, respectively. A similar trend was observed for the absorption spectra of HIAM-0022 to HIAM-0025 with an absorption edge beyond 700 nm (Fig. 2b). Based on the Tauc plots shown in Fig. 2c, the bandgaps (E_g) were calculated to be 1.80, 1.71, 1.69 and 1.72 eV for HIAM-0022, HIAM-0023, HIAM-0024 and HIAM-0025, respectively. According to the Mott–Schottky measurements (Fig. S19, ESI†), the corresponding energies of conduction bands (E_{CB}) were determined to be −0.51, −0.59, −0.61 and −0.65 V (*vs.* a normal hydrogen electrode, NHE). Combining E_g and E_{CB}, the energies of valence bands (E_{VB}) of HIAM-0022, HIAM-0023, HIAM-0024 and HIAM-0025 were determined to be 1.29, 1.12, 1.08 and 1.07 V (*vs.* NHE) as depicted in energy band structure diagrams in Fig. 2d. To further evaluate the electrochemical behaviours of HIAM-0022 to HIAM-0025, electrochemical impendence spectroscopy (EIS) and transient photocurrent responses were utilized to investigate their charge carrier transport and separation ability. As shown in Fig. 2e, the order of radii in the EIS for these for COFs is HIAM-0022 < HIAM-0023 < HIAM-0024 < HIAM-0025, indicative of the lowest resistance of charge transfer of HIAM-0022. Meanwhile, HIAM-0023 possesses higher photocurrent density compared to the other three COFs (Fig. 2f), which implies better charge separation ability for HIAM-0023.

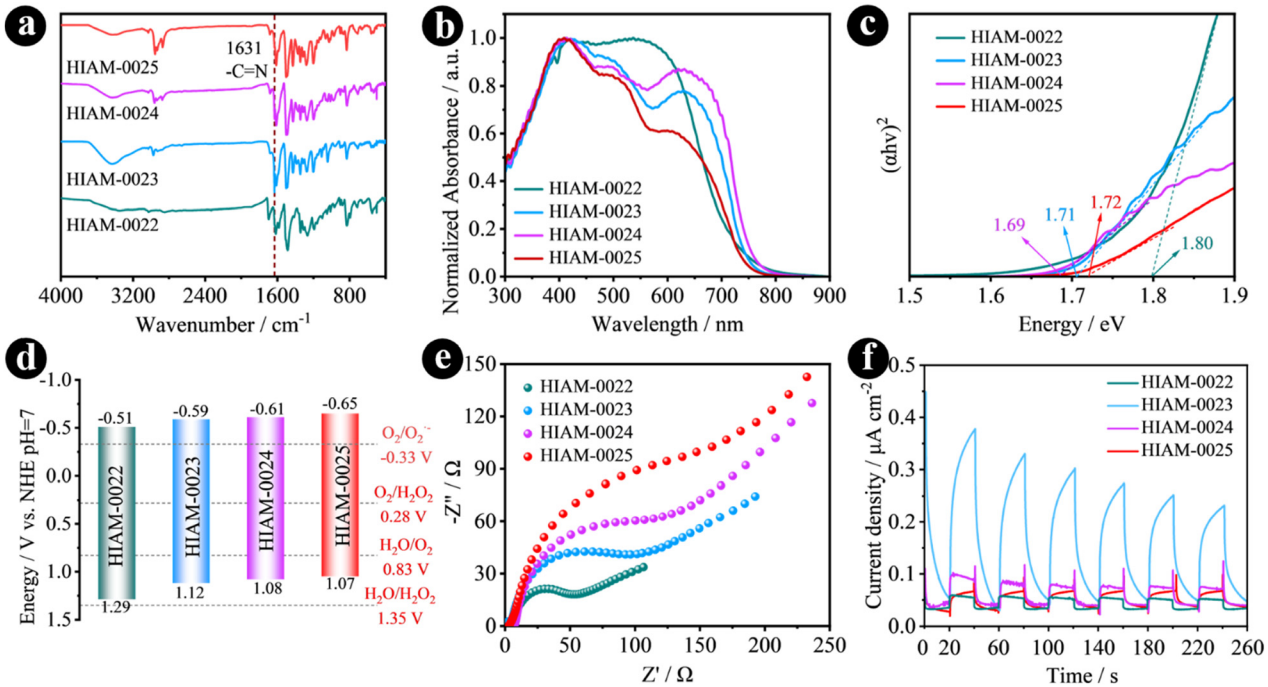

Fig. 2 FT-IR spectra (a), UV-vis spectra (b), Tauc plots (c), schematic energy band structures (d), electrochemical impedance spectra (e) and transient photocurrents of (f) HIAM-0022, HIAM-0023, HIAM-0024 and HIAM-0025.

Encouraged by the excellent chemical stability and suitable electronic structures for O_2 reduction and H_2O oxidation of HIAM-0022 to HIAM-0025 (Fig. 2d), their photocatalytic activities toward H_2O_2 generation were explored without adding any sacrificial reagents in water and air under Xe lamp irradiation ($\lambda > 420$ nm). As depicted in Fig. 3a, among these four COFs, HIAM-0023 exhibits the best catalytic efficiency for H_2O_2 photosynthesis compared with the other three COFs with H_2O_2

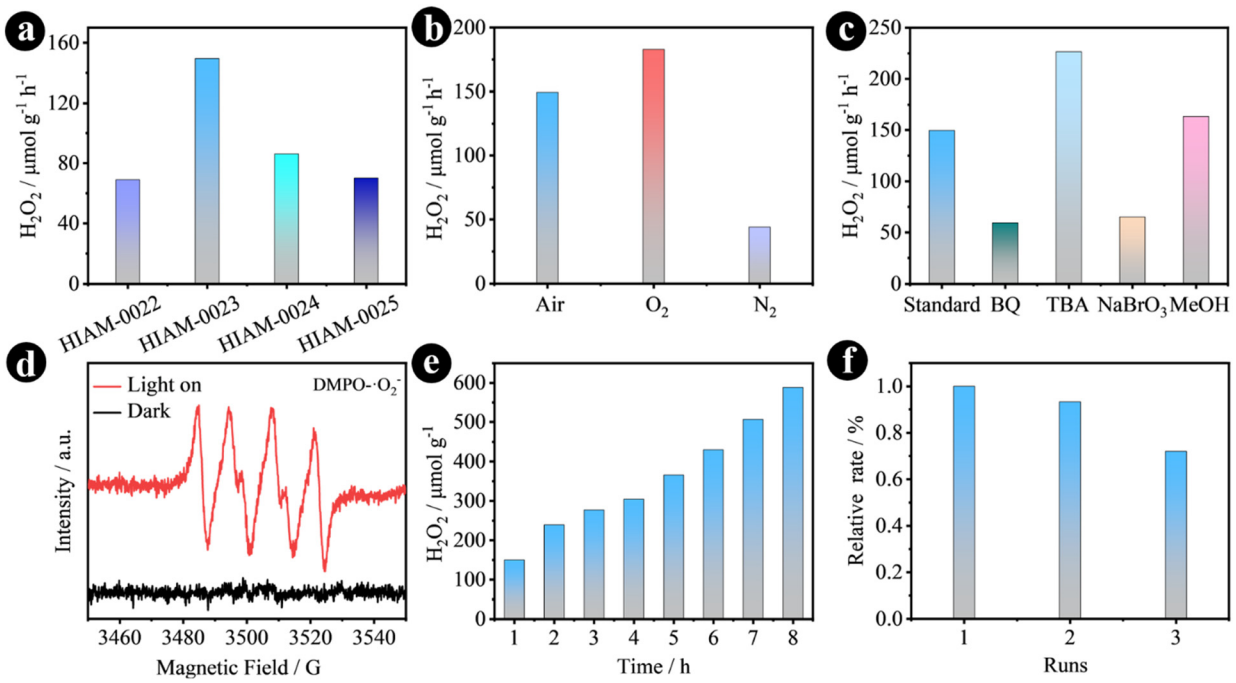

Fig. 3 Photocatalytic performance in H_2O_2 production by HIAM-0022, HIAM-0023, HIAM-0024 and HIAM-0025 under pure water and air atmospheres and Xe lamp irradiation (a). Photocatalysis experiments of HIAM-0023 under different conditions (b). Trapping experiments of HIAM-0023 for H_2O_2 photosynthesis (c). The DMPO spin trapping EPR spectra of HIAM-0023 under dark and visible light conditions (d). The long-term photocatalytic reaction (e) and photocatalytic repeatability (f) of HIAM-0023.

generated rates of 68.9, 149.5, 86.1 and 70.1 μmol g^{-1} h^{-1} for HIAM-0022, HIAM-0023, HIAM-0024 and HIAM-0025, respectively. To gain a deep understanding about the H_2O_2 generation mechanism, a series of control experiments were carried out using HIAM-0023. The photocatalytic H_2O_2 generation rates in the O_2 and N_2 atmospheres were 182.7 and 44.1 μmol g^{-1} h^{-1} (Fig. 3b), respectively, suggesting that photocatalytic H_2O_2 evolution governed by the $2e^-$ O_2 reduction reaction and water oxidation reaction hardly contributes to H_2O_2 generation. As shown in Fig. 3c, H_2O_2 generation rates obviously decreased to 59.3 and 65.0 μmol g^{-1} h^{-1} when benzoquinone (BQ, trapping agent of $^{\bullet}O_2^-$) and $NaBrO_3$ (trapping agent of electrons) were added into the photocatalytic system, respectively. When *tert*-butanol (TBA, trapping agent of $^{\bullet}OH$) was added, an increased rate of 226.5 μmol g^{-1} h^{-1} was obtained, which illustrates that $^{\bullet}OH$ did not participate in the photocatalytic reaction system. Similarly, an enhanced performance was recorded when methanol was added as a sacrificial reagent like TBA. The $2e^-$ O_2 reduction reaction was further confirmed by the electron paramagnetic resonance (EPR) experiment, where the typical characteristic signals for $^{\bullet}O_2^-$ are observed under visible-light irradiation for HIAM-0023 (Fig. 3d).

The amount of generated H_2O_2 gradually increased with continuous irradiation and reached up to 2.94 mmol after 8 hours (Fig. 3e). The resultant H_2O_2 solution can be directly used to degrade rhodamine. The color of rhodamine solution became faint in a few seconds and eventually turned colorless (Fig. S20a, ESI†), which was confirmed by the significant decrease in the UV-vis absorption spectra of rhodamine solution (Fig. S20b, ESI†). The generation efficiency of H_2O_2 was gradually reduced after three cycles, which might be ascribed to the loss of COFs during recovery (Fig. 3f). After the photocatalytic reaction, no significant change was recorded for the PXRD patterns and FT-IR spectra of HIAM-0022 to HIAM-0025 (Fig. S21 and S22, ESI†), which further indicated their high stability for practical applications.

Synthesis, characterization and hydrogen peroxide production performances of partially hydroxylated HIAM-0023

As reported, the mixed-linker strategy has been used as an efficient approach to increase the photocatalytic activities of COFs.[34,35] Therefore, to realize an enhanced photocatalytic H_2O_2 generation performance, 2,5-dihydroxyterephthalaldehyde (DHTA) was introduced to synthesize partially hydroxylated HIAM-0023, which was named HIAM-0023-*X*% (*X*% is the molar percentage of DHTA for the synthesis and *X* = 12.5, 25.0, 37.5 and 50.0). HIAM-0023-*X*% was synthesized from the solvothermal acid-catalyzed three-component reaction, in which DHTA and DETA with different molar ratios reacted with BTAPA to obtain HIAM-0023 with different degrees of hydroxylation (Fig. 4a). The well-matched PXRD patterns and FT-IR spectra indicated the successful formation of four kinds of HIAM-0023-*X*% (Fig. 4b, c and Fig. S23, ESI†), which is further confirmed by the solid-state ^{13}C NMR spectra (Fig. S24, ESI†). The ^1H solution-state nuclear magnetic resonance (^1H NMR) was conducted to determine the exact composition of HIAM-0023-*X*%, where these COFs were activated and digested using acids. As shown in Table S1 and Fig. S25–S28 (ESI†), the output molar ratios of DHTA and DETA are 1 : 6.4, 1 : 2.06, 1 : 1.19 and 1 : 0.42 for HIAM-0023-12.5%, HIAM-0023-25.0%, HIAM-0023-37.5% and HIAM-0023-50.0%,

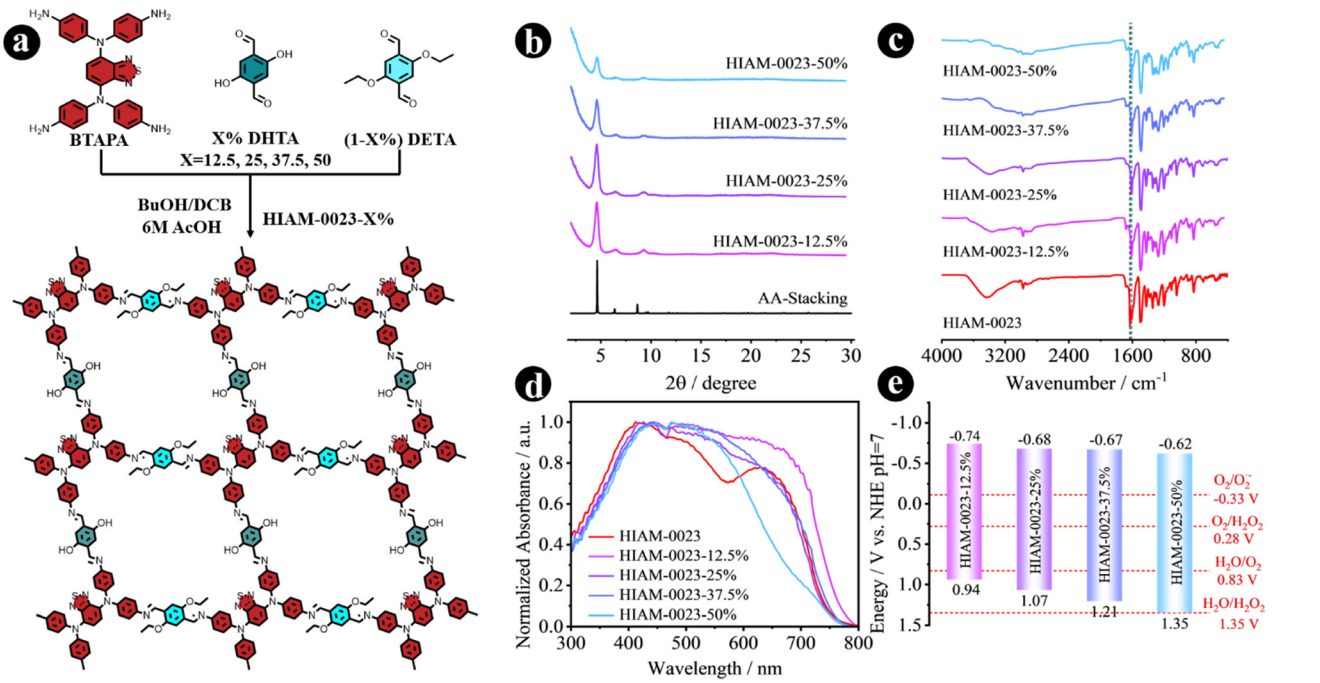

Fig. 4 Molecular structures of organic building units and synthesis conditions of HIAM-0023-*X*% (a). PXRD patterns (b), FT-IR spectra (c), solid-state UV-vis spectra (d) and the schematic energy band structure (e) of HIAM-0023-*X*%.

respectively. The UV-vis spectra were recorded with a gradual blue-shift with the increased concentration of DHTA (Fig. 4d), with which the E_g values of HIAM-0023-12.5%, HIAM-0023-25.0%, HIAM-0023-37.5% and HIAM-0023-50.0% were calculated to be 1.67, 1.75, 1.88 and 1.97 eV, respectively (Fig. S29, ESI†). According to the Mott–Schottky plots (Fig. S30, ESI†), the corresponding flat band potentials were estimated to be −0.96, −0.90, −0.89 and −0.84 V (*vs.* Ag/AgCl). Then, the E_{CB} levels were determined to be −0.74, −0.68, −0.67 and −0.62 V (*vs.* NHE). Consequently, the E_{VB} levels were estimated to be 0.94, 1.07, 1.21 and 1.35 V (*vs.* NHE) as shown in energy band structure diagrams in Fig. 4e for HIAM-0023-12.5%, HIAM-0023-25.0%, HIAM-0023-37.5% and HIAM-0023-50.0%, respectively. The porosity and pore size distribution of HIAM-0023-*X*% were evaluated using CO_2 adsorption–desorption analysis (Fig. S31, ESI†).

Under the same test conditions as HIAM-0023, the photocatalytic H_2O_2 generation rates were determined to be 264.0, 307.3, 391.7 and 246.0 μmol g^{-1} h^{-1} for HIAM-0023-12.5%, HIAM-0023-25.0%, HIAM-0023-37.5% and HIAM-0023-50.0% (Fig. 5a), respectively, which are much higher than that of HIAM-0023. The highest photocatalytic activity of HIAM-0023-37.5% might be ascribed to its better charge separation ability as confirmed by its higher transient photocurrent response compared with the other three COFs (Fig. S32, ESI†). The H_2O_2 generation rate was slightly increased to 506.3 μmol g^{-1} h^{-1} in pure O_2 and remarkably decreased to 40.1 μmol g^{-1} h^{-1} in pure N_2 for HIAM-0023-37.5% (Fig. 5b), indicating that H_2O_2 evolution is a $2e^-$ O_2 reduction process. The remarkably decreased generation rates were recorded for HIAM-0023-37.5% when BQ and $NaBrO_3$ were added into the photocatalytic system, which increased to 474.9 and 436.6 μmol g^{-1} h^{-1} with TBA and methanol as sacrificial reagents (Fig. 5c). The $2e^-$ O_2 reduction reaction using $^{\bullet}O_2^-$ as the intermediate was confirmed by the EPR experiment (Fig. 5d). Although the photocatalytic performances of these COFs are lower than those reported in most works (Table S6, ESI†), the main aim of the present work has been achieved to investigate topological effects on the photocatalytic efficiency of resultant COFs.

To have a further understanding about the mechanism for H_2O_2 generation, the ORR and WOR processes were investigated through rotating disk electrode (RDE) and rotating ring-disk electrode (RRDE) experiments. RDE analysis indicated that the average electron transfer numbers for HIAM-0023-12.5%, HIAM-0023-25.0%, HIAM-0023-37.5% and HIAM-0023-50.0% were determined to be 2.27, 2.01, 2.10 and 2.13 in the oxygen reduction reaction, respectively (Fig. 5e and Fig. S33, S34, ESI†). In the RRDE experiments, weak reduction currents were observed when the Pt ring electrode was set at −0.23 V (Fig. 5f), illustrating that these four COFs can generate O_2 in the WOR process. Meanwhile, no oxidation current was recorded when the Pt ring electrode was set at 0.6 V (Fig. S35, ESI†), which demonstrates that no H_2O_2 can be generated. Based on the aforementioned results, it is clear that the photocatalytic H_2O_2 generation process is the combination of

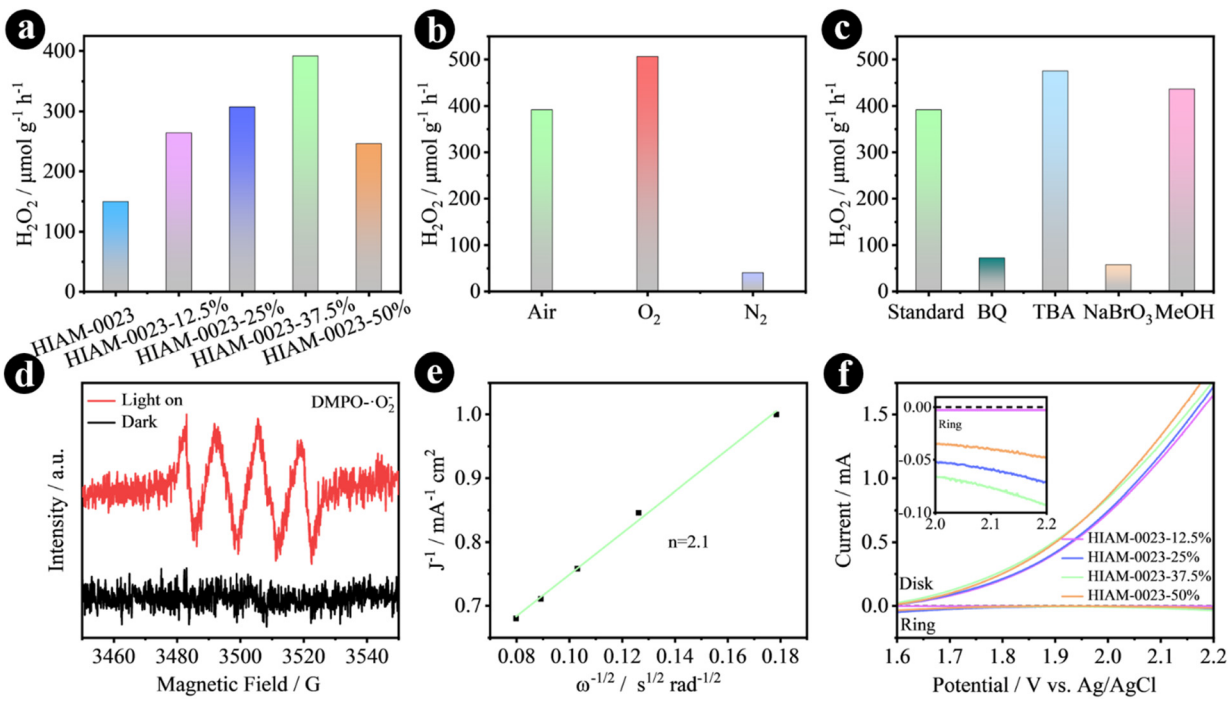

Fig. 5 Photocatalytic performances of H_2O_2 production by HIAM-0023-*X*% in the pure water and air atmosphere under Xe lamp irradiation (a). Photocatalysis experiments of HIAM-0023-37.5% under different conditions (b). Trapping experiments of HIAM-0023-37.5% for H_2O_2 photosynthesis (c). The DMPO spin trapping EPR spectra of HIAM-0023-37.5% under dark and visible light (d). Koutecky–Levich plots of HIAM-0023-37.5% obtained by RDE measurements at −1.2 V (*vs.* Ag/AgCl) (e). The RRDE measurements of HIAM-0023-*X*% with a rotating speed of 1600 rpm (the potential of the Pt ring electrode was set at −0.23 V (*vs.* Ag/AgCl) to detect O_2) (f).

the $2e^-$ oxygen reduction reaction and one-step $4e^-$ water oxidation.

Conclusions

In summary, we have successfully synthesized two kinds of COFs with **kgm** and **fes** underlying nets *via* tuning the side-chain length of organic building units, which exhibit significant differences for H_2O_2 photosynthesis. The ethoxy group-based **fes** COF, HIAM-0023, exhibits 2.2 times higher H_2O_2 generation rate (149.5 μmol g^{-1} h^{-1}) than non-substituted **kgm** type COFs. In addition, enhanced photocatalytic performances are obtained for partially hydroxylated HIAM-0023. HIAM-0023-37.5% shows the highest photocatalytic H_2O_2 generation rate of 391.7 μmol g^{-1} h^{-1}, which is 2.6 times higher than that of HIAM-0023 and 5.7 times higher than that of HIAM-0022 with the **kgm** underlying net. The higher photocatalytic activities can be attributed to the better charge separation ability of corresponding COFs. This work sheds light on the rational construction of COFs with controllable topologies and compositions to realize efficient H_2O_2 generation.

Data availability

The data that support the findings of this study are available from the corresponding author upon reasonable request.

Conflicts of interest

There are no conflicts to declare.

Acknowledgements

X.-Y. Liu acknowledges the financial support from start-up funding for Shenzhen High-Caliber Personnel of Shenzhen Polytechnic University (6022310053K).

References

1 C. S. Diercks and O. M. Yaghi, *Science*, 2017, **355**, eaal1585.
2 S. Kandambeth, K. Dey and R. Banerjee, *J. Am. Chem. Soc.*, 2019, **141**, 1807–1822.
3 Y. Song, Q. Sun, B. Aguila and S. Ma, *Adv. Sci.*, 2019, **6**, 1801410.
4 K. T. Tan, S. Ghosh, Z. Wang, F. Wen, D. Rodríguez-San-Miguel, J. Feng, N. Huang, W. Wang, F. Zamora, X. Feng, A. Thomas and D. Jiang, *Nat. Rev. Methods Primers*, 2023, **3**, 1.
5 Y.-N. Gong, X. Guan and H.-L. Jiang, *Coord. Chem. Rev.*, 2023, **475**, 214889.
6 D. Tan, R. Zhuang, R. Chen, M. Ban, W. Feng, F. Xu, X. Chen and Q. Wang, *Adv. Funct. Mater.*, 2023, 2311655.
7 Z. Yong and T. Ma, *Angew. Chem., Int. Ed.*, 2023, **62**, e202308980.
8 C. Krishnaraj, H. Sekhar Jena, L. Bourda, A. Laemont, P. Pachfule, J. Roeser, C. V. Chandran, S. Borgmans, S. M. J. Rogge, K. Leus, C. V. Stevens, J. A. Martens, V. Van Speybroeck, E. Breynaert, A. Thomas and P. Van Der Voort, *J. Am. Chem. Soc.*, 2020, **142**, 20107–20116.
9 S. Chai, X. Chen, X. Zhang, Y. Fang, R. S. Sprick and X. Chen, *Environ. Sci.: Nano*, 2022, **9**, 2464–2469.
10 M. Kou, Y. Wang, Y. Xu, L. Ye, Y. Huang, B. Jia, H. Li, J. Ren, Y. Deng, J. Chen, Y. Zhou, K. Lei, L. Wang, W. Liu, H. Huang and T. Ma, *Angew. Chem., Int. Ed.*, 2022, **61**, e202200413.
11 Q. Zhi, W. Liu, R. Jiang, X. Zhan, Y. Jin, X. Chen, X. Yang, K. Wang, W. Cao, D. Qi and J. Jiang, *J. Am. Chem. Soc.*, 2022, **144**, 21328–21336.
12 J.-N. Chang, Q. Li, J.-W. Shi, M. Zhang, L. Zhang, S. Li, Y. Chen, S.-L. Li and Y.-Q. Lan, *Angew. Chem., Int. Ed.*, 2023, **62**, e202218868.
13 D. Chen, W. Chen, Y. Wu, L. Wang, X. Wu, H. Xu and L. Chen, *Angew. Chem., Int. Ed.*, 2023, **62**, e202217479.
14 P. Das, G. Chakraborty, J. Roeser, S. Vogl, J. Rabeah and A. Thomas, *J. Am. Chem. Soc.*, 2023, **145**, 2975–2984.
15 J. Sun, H. Sekhar Jena, C. Krishnaraj, K. Singh Rawat, S. Abednatanzi, J. Chakraborty, A. Laemont, W. Liu, H. Chen, Y.-Y. Liu, K. Leus, H. Vrielinck, V. Van Speybroeck and P. Van Der Voort, *Angew. Chem., Int. Ed.*, 2023, **62**, e202216719.
16 Y. Zhang, Z. Qiao, R. Zhang, Z. Wang, H.-J. Wang, J. Zhao, D. Cao and S. Wang, *Angew. Chem., Int. Ed.*, 2023, **62**, e202314539.
17 Y. Chen, R. Liu, Y. Guo, G. Wu, T. C. Sum, S. W. Yang and D. Jiang, *Nat. Synth.*, 2024, **3**, 998–1010.
18 R. Liu, Y. Chen, H. Yu, M. Položij, Y. Guo, T. C. Sum, T. Heine and D. Jiang, *Nat. Catal.*, 2024, **7**, 195–206.
19 H. Xu, S. Xia, C. Li, Y. Li, W. Xing, Y. Jiang and X. Chen, *Angew. Chem., Int. Ed.*, 2024, **63**, e202405476.
20 H. Yu, F. Zhang, Q. Chen, P.-K. Zhou, W. Xing, S. Wang, G. Zhang, Y. Jiang and X. Chen, *Angew. Chem., Int. Ed.*, 2024, **63**, e202402297.
21 Q. Liao, Q. Sun, H. Xu, Y. Wang, Y. Xu, Z. Li, J. Hu, D. Wang, H. Li and K. Xi, *Angew. Chem., Int. Ed.*, 2023, **62**, e202310556.
22 F. Liu, P. Zhou, Y. Hou, H. Tan, Y. Liang, J. Liang, Q. Zhang, S. Guo, M. Tong and J. Ni, *Nat. Commun.*, 2023, **14**, 4344.
23 Y. Mou, X. Wu, C. Qin, J. Chen, Y. Zhao, L. Jiang, C. Zhang, X. Yuan, E. Huixiang Ang and H. Wang, *Angew. Chem., Int. Ed.*, 2023, **62**, e202309480.
24 J.-Y. Yue, L.-P. Song, Y.-F. Fan, Z.-X. Pan, P. Yang, Y. Ma, Q. Xu and B. Tang, *Angew. Chem., Int. Ed.*, 2023, **62**, e202309624.
25 J.-N. Chang, J.-W. Shi, Q. Li, S. Li, Y.-R. Wang, Y. Chen, F. Yu, S.-L. Li and Y.-Q. Lan, *Angew. Chem., Int. Ed.*, 2023, **62**, e202303606.
26 R. R. Liang, F. Z. Cui, Q. Y. Qi and X. Zhao, *CCS Chem.*, 2020, **2**, 139–145.
27 Y. Li, L. Guo, Y. Lv, Z. Zhao, Y. Ma, W. Chen, G. Xing, D. Jiang and L. Chen, *Angew. Chem., Int. Ed.*, 2021, **60**, 5363–5369.
28 Z. Zhao, J. Zhao, S. Zhang, G. Zhang, W. Chen, Z. Yang, T. Zhang and L. Chen, *Nanoscale*, 2021, **13**, 19385–19390.
29 T. Ma, J. Li, J. Niu, L. Zhang, A. S. Etman, C. Lin, D. Shi, P. Chen, L.-H. Li, X. Du, J. Sun and W. Wang, *J. Am. Chem. Soc.*, 2018, **140**, 6763–6766.

30 Y.-P. Mo, X.-H. Liu and D. Wang, *ACS Nano*, 2017, **11**, 11694–11700.
31 Z.-F. Pang, T.-Y. Zhou, R.-R. Liang, Q.-Y. Qi and X. Zhao, *Chem. Sci.*, 2017, **8**, 3866–3870.
32 Y. Peng, L. Li, C. Zhu, B. Chen, M. Zhao, Z. Zhang, Z. Lai, X. Zhang, C. Tan, Y. Han, Y. Zhu and H. Zhang, *J. Am. Chem. Soc.*, 2020, **142**, 13162–13169.
33 Z. Shan, M. Wu, T. Liu, J. Wang, C. Chen, S. Li, J. Su and G. Zhang, *ACS Appl. Mater. Interfaces*, 2023, **15**, 35350–35357.
34 H. Wang, C. Yang, F. Chen, G. Zheng and Q. Han, *Angew. Chem., Int. Ed.*, 2022, **61**, e202202328.
35 C. Shu, X. Yang, L. Liu, X. Hu, R. Sun, X. Yang, A. I. Cooper, B. Tan and X. Wang, *Angew. Chem., Int. Ed.*, 2024, **63**, e202403926.